Chapter II

THE COMPTEL INSTRUMENT

A new era in gamma-ray astronomy began in April 1991 with the successful launch and deployment of the Compton Gamma Ray Observatory (CGRO). Orbiting the Earth at a nominal height of 450 km, the *Compton* mission goals include performing the first full-sky survey in gamma rays. With four different instruments, *Compton* operates over a wide range of photon energies from about 5 keV to 20 GeV.

The Imaging Compton Telescope COMPTEL, on-board CGRO, is an imaging wide-field gamma-ray telescope sensitive to photons between 1 and 30 MeV, a poorly explored energy regime. COMPTEL is the first Compton telescope to be placed in orbit allowing us to conduct gamma-ray observations for extended periods of time. Some of its primary goals are to provide the first all-sky survey at these energies and search for new gamma-ray sources, to observe known galactic and extragalactic sources (e.g. pulsars, x-ray binaries, AGNs, Supernovae, GRB, etc.) and measure the diffuse continuum and line emission from the Galaxy. Due to its large detection area, wide field-of-view, long observation times and low background, COMPTEL is also well suited to study the Cosmic Diffuse Gamma (CDG) radiation.

II.A. Principle of Measurement

Medium energy gamma rays are loosely defined as those photons in the energy range of 1 to 30 MeV. This is above the electron-positron annihilation energy (0.511 MeV) and below that of the π^0-meson decay energy (~68 MeV). The primary interaction between matter and photons at these energies is the Compton-scattering process with a relatively small cross-section. Thus, medium energy gamma rays are penetrating and can propagate great distances in the Universe without scattering. Ironically, the process that makes these photons so valuable to study astrophysics also makes them difficult to detect and measure.

The detection problem for medium energy gamma rays has led to the development of *Compton telescopes*. These are gamma-ray detectors in which the Compton-scattering process is used to measure the incident photon energy and direction. Prior to the development of COMPTEL, Compton telescopes were designed and developed by research groups at MPE (Schönfelder, Hirner, and Schneider 1973), UCR (Herzo 1975) and UNH (Lockwood et al. 1981). As a Compton telescope, COMPTEL shares the basic principle of detection with these earlier instruments (Ryan 1989, Schönfelder et al. 1984).

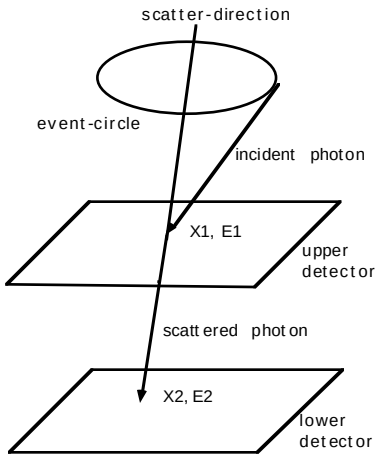

Figure II.1 The principle of measurement for a Compton telescope.

In a Compton telescope, the incident photon must interact in two physically independent detector elements, usually a Compton-scatter from one detector into another, to register a valid event. The basic scattering process is illustrated in figure II.1. The basic quantities measured are the interaction locations (X1 and X2) and the energy deposits (E1 and E2) in the upper (D1) and lower (D2) detector planes, respectively. Ideally, the scattered electron (in D1) and the scattered photon (in D2) are totally absorbed with a measurement of the interaction positions. The time-of-flight measurement establishes the general upward or downward direction for the photon. The total energy (ETOT) and the scatter-angle of the incident photon (ϕ) is computed from the Compton scatter kinematics.

$$ETOT = E1 + E2 \tag{2.1}$$

$$\phi = \cos^{-1}\left[1 - m_e c^2\left(\frac{1}{E2} - \frac{1}{E1+E2}\right)\right] \tag{2.2}$$

The incident photon can arrive from any position along the mantle of the cone of half-angle ϕ centered along the scattered-photon direction (the vector through X1 and X2). The origin of the detected photon lies along the projection of this cone in the sky and is usually referred to as an *event circle*. The azimuth direction information of the incident photon is solely contained in the direction of the scattered electron in the upper detector. This is not measured and hence leads to an azimuthal degeneracy in the reconstruction of the incident photon direction, i.e., an event circle instead of an event-location.

Although the requirement of coincidence greatly reduce the background contribution to the measured count rate, it simultaneously reduce the overall detection efficiency. Consequently, Compton telescopes are generally large to compensate for the reduced efficiency while retaining a relatively high signal-to-background ratio.

In a real instrument, there are many measurement errors that lead to uncertainties in the measurement of the photon direction and energy. The uncertainties in the interaction location lead to uncertainties in the direction of the cone-axis (scatter direction), while the uncertainties in the energy deposits lead to uncertainties in the computed scatter angle. These combined effects lead to a thick *event annulus* rather than a thin event circle for the possible incident photon directions.

II.B. Instrument Description

A detailed description of the COMPTEL instrument and its operation was presented by Schönfelder et al. (1993). The schematic design of the COMPTEL instrument is shown in figure II.2. It consists of two layers (or arrays) of scintillating modules separated by 1.58 meters. The upper detector plane, called D1, consists of seven modules that are filled with liquid scintillator (NE213A), with properties of low Z ($CH_{1.2}$) and low density (ρ ~1 g/cm^3). With a thickness of 8.5 cm, the D1 design optimizes the probability of a single Compton scatter within a single D1 module. Each of the D1 modules is viewed by eight photo-multiplier tubes (PMTs) spaced regularly around the module. The D1 modules are mounted on a thin aluminum plate 1.45 m in diameter with holes cut out beneath the D1 modules. The high-voltage power supplies, the high-voltage junction boxes and the front-end electronics are mounted beneath the platform out of the gamma-ray path from D1 to D2. Each of the modules also has a scintillator expansion chamber mounted on top of the platform. The D1 detector assembly has an active area of 4188 cm^2.

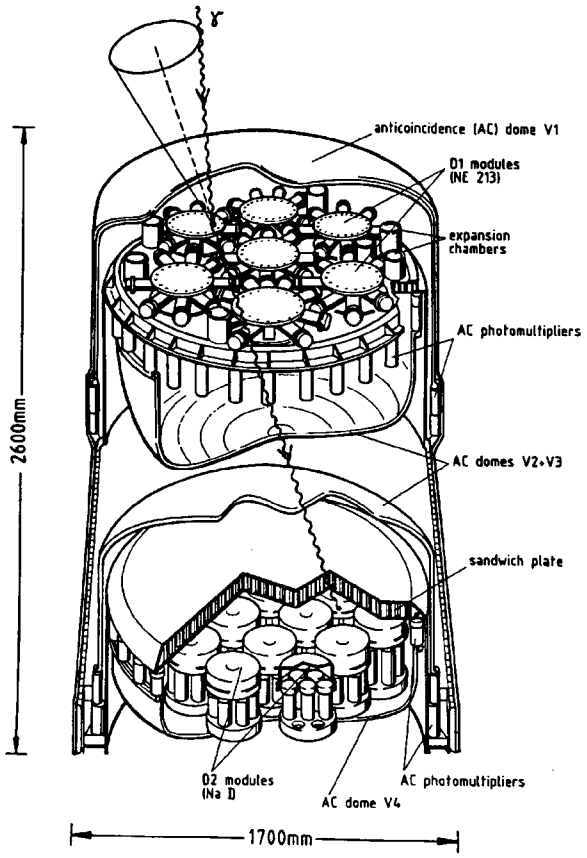

Figure II.2 A schematic diagram of COMPTEL.

The lower detector plane, called D2, consists of fourteen modules made of scintillating inorganic NaI(Tl) crystals, with properties of high Z to absorb the scattered photons. Each of the D2 modules is viewed by seven PMTs from below. The D2 modules are attached to the bottom of a 20 mm thick Al honeycomb sandwich plate (0.22 g/cm^2 above the D2 modules). The D2 detector assembly has an active area of 8744 cm^2.

The interaction location and the energy deposit within individual modules are indirectly determined from the distribution of scintillator light collected by the PMTs viewing each module. The PMT gains that are used to convert the summed PMT signals to energy deposits, are monitored using a ^{60}Co calibration system. The D1 and D2 position resolution is 2-dimensional, no depth measurement is made.

The instrument operates in the range of 800 keV to 30 MeV with a field-of-view of ~1.5 steradians. The total energy resolution (FWHM) improves with energy from about 10% at 1 MeV to 5% at 20 MeV. The spatial resolution (1σ) at 1 MeV is approximately 2 cm for a D1 module

and 1 cm for a D2 module. These energy and spatial resolutions translate through the Compton-scatter kinematics to an angular resolution of 1–2˚, again a function of total energy and zenith angle.

Each of the D1 and D2 detector subsystems is completely surrounded by two active plastic charged-particle shields (veto domes) that are used in anti-coincidence with D1 and D2 detectors to reject charged-particle triggers. Each of the four Cassini-shaped veto domes (see figure II.2) is made of thin plastic scintillator (1.5 cm thick) and viewed by 24 PMTs. The veto domes do not significantly attenuate the external gamma ray flux, yet are nearly 100% efficient in detecting charged particles. In order to allow for overlap, the two domes surrounding each detector assembly have different sizes; the larger dome on top with the smaller dome below. See section II.G for additional details on the veto system.

The D1 detector modules also possess pulse-shape-discrimination (PSD) properties, in that proton ionization tracks produce pulses with slow rise times in their emitted scintillator light compared to the scintillator pulses from electrons and other minimum ionizing particles. The raw PSD pulses depend on the total energy deposit within the module. After removing the energy dependence, the gamma-ray events cluster around channel 80 in the PSD parameter. The neutron-induced events are usually found above channel 100. This allows us to suppress events produced by fast neutrons scattering off the hydrogen or the carbon in the D1 scintillator where the signals from recoil or knock-on protons trigger the D1 module.

COMPTEL also measures the time sequence of the D1 and D2 interaction with the time-of-flight (ToF) system. The ToF measurement is defined as the time difference between the interactions in the D1 and D2 modules. The measured ToF values are set by the coincidence-time window that has an adjustable offset. The coincidence time window is fixed at ~40 ns and the measured raw ToF is expressed in channels 0–255 with 1 channel corresponding to 0.26 ns in ToF. The ToF settings have been stable since launch with zero ToF value set at channel 100 and the measured ToF values ranging from channels 40 to 200. The raw ToF values are used by the onboard electronics to distinguish down-scattered or forward-scattered events (D1→D2) from up-scattered (D2→D1) events. We refer to the down-scattered events as Gamma-1 events that are used in scientific analysis. The up-scattered events labeled Gamma-2 events are identified

onboard and telemetered separately with lower priority. The absolute time of the event is recorded with an accuracy of 125 μs. See sections II.F and V.A for more details on the ToF measurement. The ToF and veto subsystems are key elements in suppressing the instrumental background events and are addressed separately.

II.C. Data Description

A COMPTEL *telescope event* is defined by a coincident signal in the upper (D1) and lower (D2) detector within the proper time-of-flight window with no signal from any of the charged-particle shields. For each event, COMPTEL measures the following: the energy deposits in D1 and D2, the interaction locations in D1 and D2, the time-of-flight between the interactions in D1 and D2, the pulse-shape of the signal in D1 and the absolute time of the event.

The processed telescope-event data are stored in so-called EVP datasets. There is an EVP dataset for each of the Gamma-1 and Gamma-2 data types. The EVP data also contain other useful information such as the veto trigger flags, the computed scatter angle and the scatter direction.

Most of the house-keeping data such as temperatures, voltages and veto-scalers are stored in HKD (house-keeping data) datasets with a time resolution of one *superpacket* (16.384 s). Some of the data represent integrations over the entire super-packet (e.g., Gamma-1 rates, Gamma-2 rates) whereas others are sampled only for a single 2.048 s packet (e.g., temperature, veto-scalers). The veto-dome trigger rates for each dome are stored in the HKD datasets.

The orbital and pointing information is stored separately in OAD (orbit-aspect data) datasets. The OAD data are also stored with super-packet resolution and contain among other things the position (latitude, longitude and altitude) of CGRO with respect to the Earth, the direction of the center of the Earth (zenith and azimuth) with respect to the CGRO coordinate system and the pointing direction in celestial coordinates.

The other important data type is the TIM dataset. These contain the start and end times of COMPTEL operation (e.g. the off and on times of COMPTEL during the passage through the South Atlantic Anomaly). Any special mode of operation and data-gaps due to telemetry loss are also recorded in the TIM datasets.

II.D. Instrument Response

The response of the COMPTEL instrument was measured prior to launch in a series of calibration runs with monoenergetic gamma-ray sources of various energies located at different geometries (Diehl et al. 1992). The results of these calibrations determine the overall performance characteristics of the instrument and all of its subsystems. Approximations used to determine the background levels and the effects of a finite source distance during calibration response measurements contribute to the overall uncertainty in the response. A Monte Carlo simulation system (the SIM subsystem) based on the CERN GEANT simulation package is used to compute the instrument response for the general case of point sources. The package uses a very detailed model of the COMPTEL mass distribution and the measured instrument characteristics from calibration, such as the individual module energy thresholds, the PSD response and the positional uncertainty, to determine the instrument response to an incident photon flux (Kippen 1991; Stacy et al. 1996).

II.D.1 Effective Area

One of the basic measures of the instrument response is the telescope effective area in units of cm^2 for point sources and cm^2-sr for diffuse sources. The effective area is the product of the intrinsic efficiency with the projected geometric-area and depends on the source direction and photon energy. The effective area (A_{eff}) is usually defined as

$$A_{eff}(\theta,\varphi,E) = A_{geo}(\theta,\varphi) \times \varepsilon(\theta,\varphi,E), \qquad (2.3)$$

where ε is the intrinsic telescope efficiency depending on the specific data selections, the incident photon direction (θ,φ) and photon energy E. A_{geo} is geometric area normal to the incident photon direction. The effective area represents the equivalent area of the instrument with 100% efficiency.

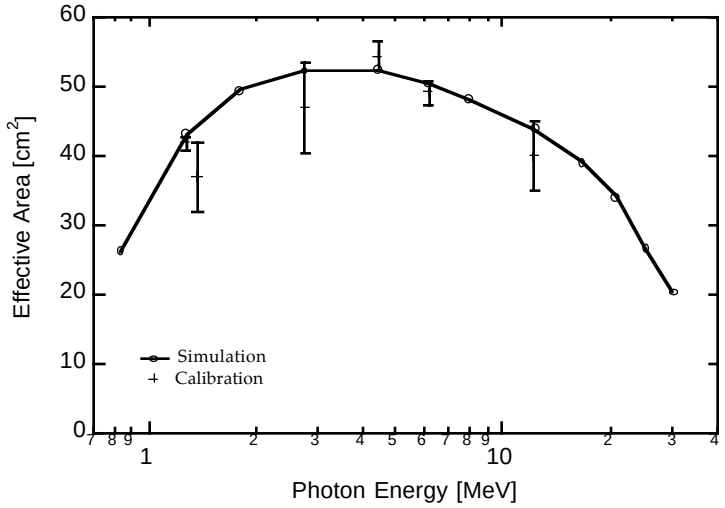

Figure II.3 A comparison between the COMPTEL effective area determined from calibration measurements and the simulation package (Stacy et al. 1996).

A comparison between the COMPTEL effective area determined from calibration measurements (see figure II.3) and the simulation package show satisfactory agreement, validating the overall SIM approach. The effective area computed using simulations is shown as a function of energy in figure II.4 for two separate event-selection criteria and two incident angles. The low energy roll-over in A_{eff} is due to the D1 and D2 module energy thresholds, while at higher energies the decrease in the Compton-scatter cross-section becomes important.

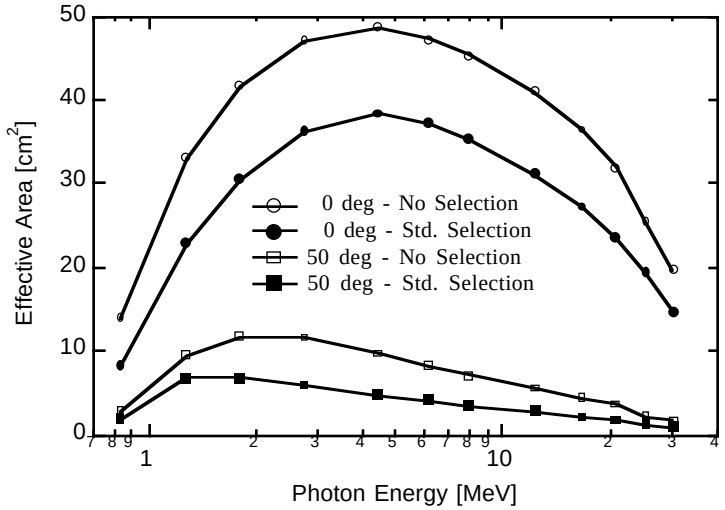

Figure II.4 The simulated COMPTEL effective area as a function of the incident photon energy for two different incidence angles.

The effective area computed using simulations as a function of zenith angle is shown in figure II.5 for two separate event-selection criteria and two different energies. The effective area

decreases roughly linearly with zenith angle. The decrease with zenith angle is associated with the decrease in the projected geometric area with increasing angle. Due to azimuthal degeneracy inherit in the measurements and the radial symmetry of the instrument, A_{eff} is only weakly dependent on azimuth.

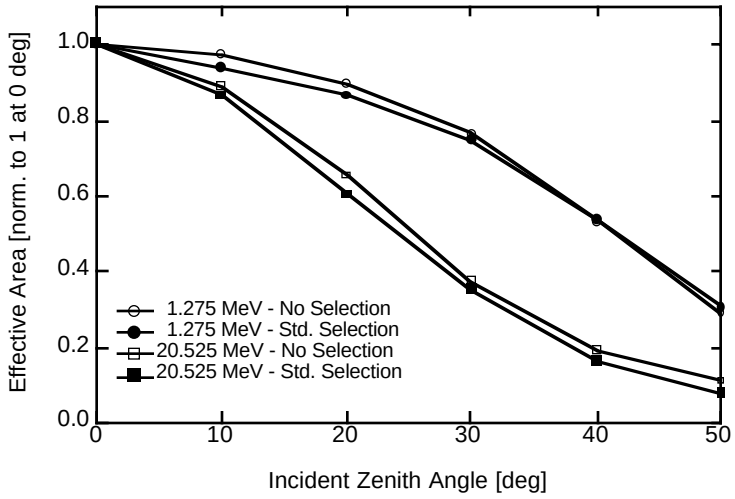

Figure II.5 The simulated COMPTEL effective area as a function of the photon incidence angle at two different energies.

II.D.2 Telescope Event Mechanism

To develop a quantitative understanding of the origin and physical mechanism of the telescope events, a detailed tracking of the simulated events was performed. Some results of this study (using the task SIMTRK) are presented here (see also Stacy et al. 1996) to illustrate the composition of the typical telescope event. The results discussed are for monoenergetic sources at normal incidence. Figure II.6 shows the fraction of scattered events to other events (when a secondary photon produced in D1 and not the scattered incident photon triggers D2). Single Compton-scattered events in D1 dominate at all energies (>80% below and >60% above 10 MeV). The fraction of non-Compton scattering events is <5–10% below 10 MeV, above which it increases to ~30% at 20–30 MeV.

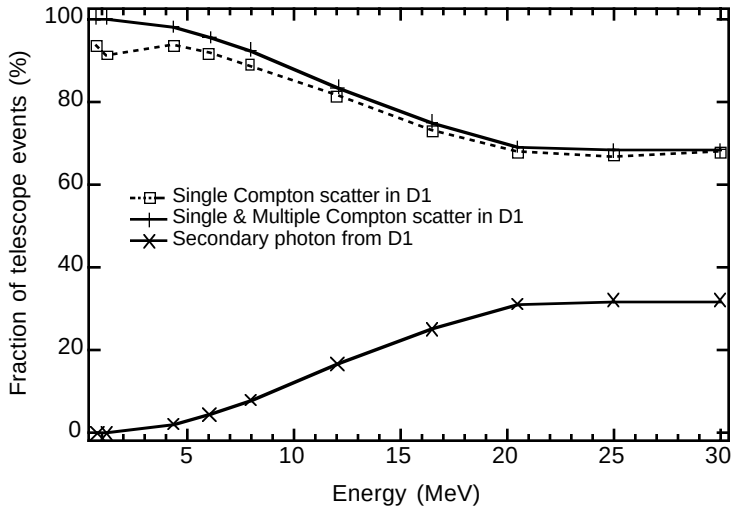

Figure II.6 The fractional composition of simulated telescope events in terms of scattered-events for normal incidence as a function of photon energy.

Telescope events can be produced through many channels or mechanisms. The events are differentiated by examining the D2 photon and sorting the event by the mechanism through which it was produced in D1. The efficiency of these mechanisms to trigger the telescope is shown in figure II.7. There are five different mechanisms that produce telescope events:

(1) The incident photon interacts through any process in D2 after Compton scattering in D1. This is the ideal case;

(2) The incident photon scatters in D1 and the bremsstrahlung photon from this Compton-scattered electron triggers D2;

(3) The incident photon pair-produces in D1 and the bremstrahlung photon from either the e^+ or e^- triggers D2;

(4) The same as (3), but the annihilation photon from the positron triggers D2;

(5) All other processes.

The leading mechanisms for the production of non-ideal events are bremstrahlung photons either from the Compton-scattered electron or from the pair-produced products of the original photon. It is important to note that the major background component in COMPTEL is not due to external photons that do not ideally interact in the detector, but rather due to internal photons that satisfy other telescope-event criteria to register valid events.

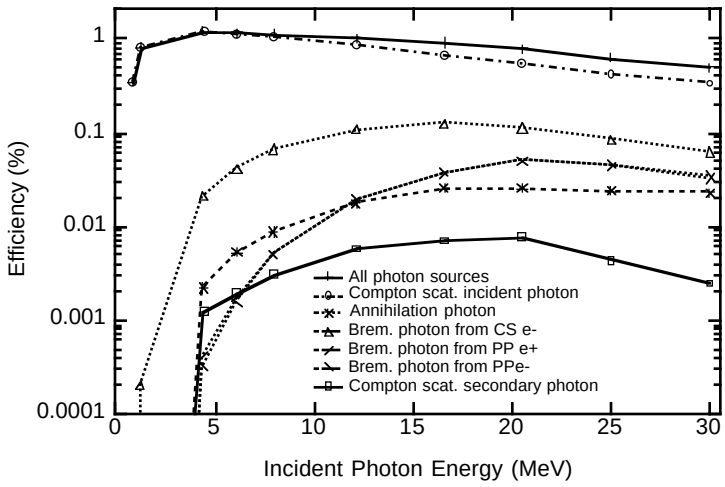

Figure II.7 Efficiency of mechanisms to produce photons in D1 that consequently trigger D2 to register valid simulated telescope events.

II.D.3 Total Energy Response

The total energy (ETOT) response of COMPTEL to a monoenergetic source is similar in character to the response of a bare NaI detector. It consists of a total energy photopeak, escape peaks and a Compton continuum. Figures II.8 and II.9 show the COMPTEL total energy response to monoenergetic point sources of 4.430 MeV and 12.140 MeV, respectively, at normal incidence.

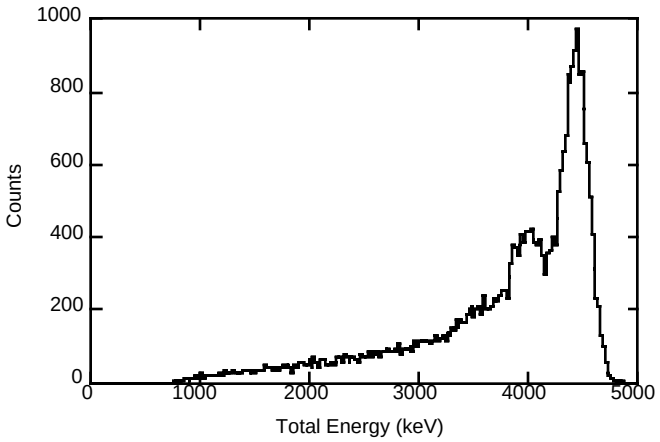

Figure II.8 The simulated total energy response of COMPTEL to a 4.430 MeV monoenergetic point source at normal incidence.

The total energy in COMPTEL is determined by the sum of the individual E1 and E2 energy deposits, corresponding to the D1 and D2 detectors, respectively. In many events either one or both of the detectors may not contain the full interaction energy, i.e., secondary photons or

particles exit the detector. As expected, the fraction of events with incomplete energy loss increases with energy. These events produce the tail in the total-energy spectrum. A detailed study of the event energy loss (figure II.10) shows that above 5 MeV there is usually escaping energy from the D2 modules. The fraction of events with escaping energy from D1 increases more slowly and becomes important (>20%) only above 10 MeV. The fraction of events with total energy absorption decreases rapidly from 60% at 1–2 MeV to ~10% at 10 MeV.

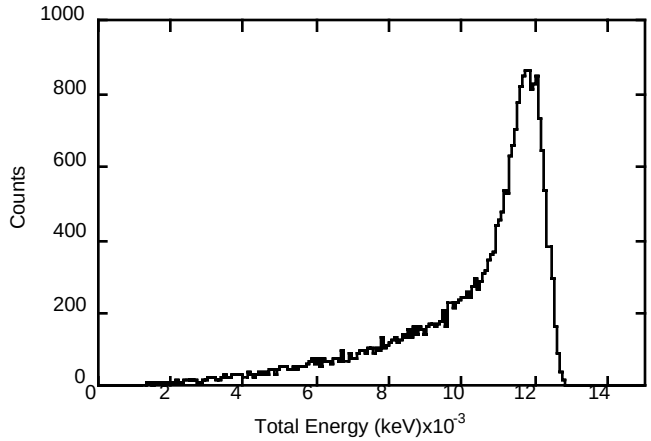

Figure II.9 The simulated total energy response of COMPTEL to a 12.140 MeV monoenergetic point source at normal incidence.

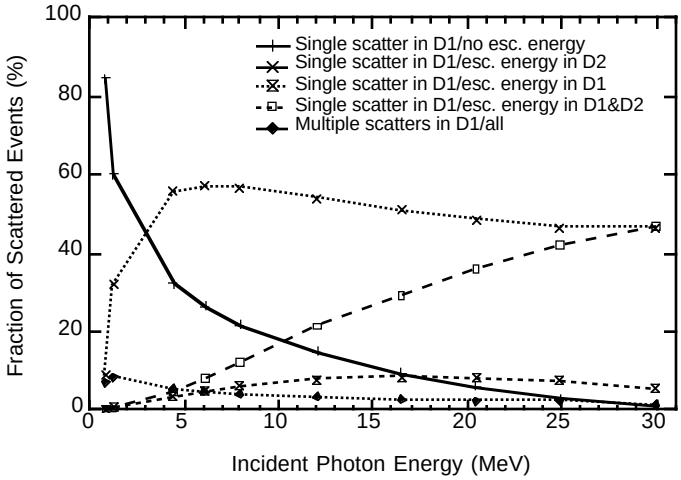

Figure II.10 The decomposition of Compton-scattered telescope events in terms of escaping energy from the D1 and D2 detectors.

II.D.4 Scatter Angle Spectrum

The quantity ϕ is a measure of the scattering angle for the incident photon after Compton scattering in D1. The ϕ distributions for 4.430 and 12.143 MeV photons at normal incidence are

shown in figures II.11 and II.12, respectively. The ϕ distribution is sensitive to the energy thresholds in D1 and D2 and the incident angle. The ϕ distribution for 4.430 MeV photons (figure II.11) shows that events that are totally absorbed peak around 5–15˚, incomplete energy deposits lead to larger ϕ values. The ϕ peak shifts to smaller angles with increasing energy (figure II.12) since the D1 threshold energy is a smaller fraction of the total energy. The non-ideal events usually have large scatter angles that are suppressed through event selections.

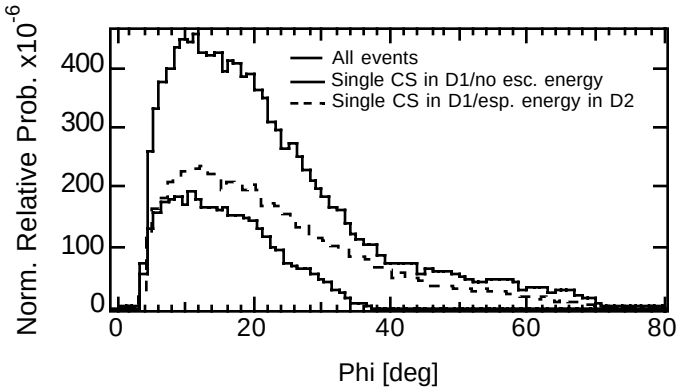

Figure II.11 The simulated ϕ spectrum for a 4.430 MeV monoenergetic point source at normal incidence.

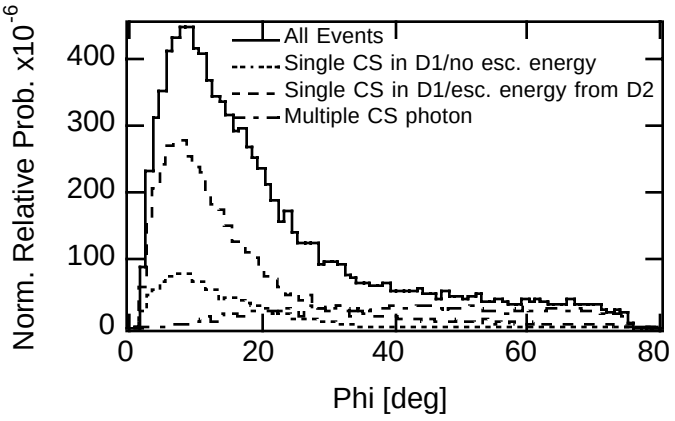

Figure II.12 The simulated ϕ spectrum for a 12.143 MeV monoenergetic point source at normal incidence.

II.D.5 ARM Distribution

Another important quantity is the angular resolution measure (ARM) defined as $\phi - \phi_{geo}$, where ϕ_{geo} is the true scatter angle and ϕ is the computed scatter angle. In the ideal case with no measurement errors, ARM will be zero. In reality, energy and location measurement errors produce a finite width of 2–3˚ in the ARM measurement distributed about zero. The ARM distribution for 4.43 and 12.143 MeV photons at normal incidence are shown in figures II.13 and

II.14, respectively. Non-ideal events and events with energy losses introduce additional asymmetries in the ARM distribution. For example, events with incomplete energy deposits in D2 generally have an artificially large ϕ value resulting in positive ARM values, while events with incomplete energy deposits in D1 generally have an artificially low ϕ value resulting in negative ARM values. Since events with escaping energy in D2 are more frequent, the typical ARM distribution has an asymmetrical excess (up to 10–15˚) toward positive ARM values .

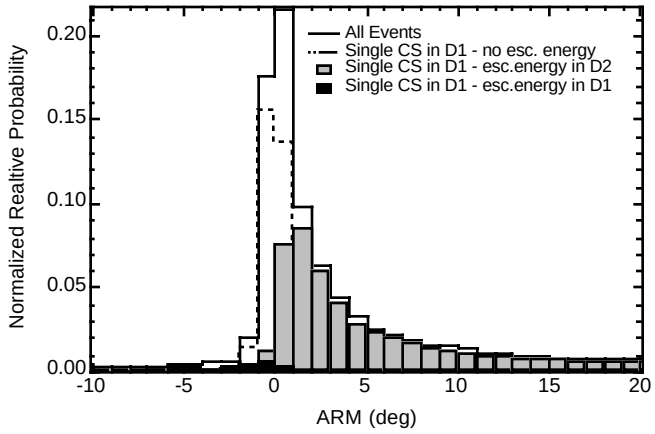

Figure II.13 The simulated ARM distribution for a 4.430 MeV monoenergetic point source at normal incidence.

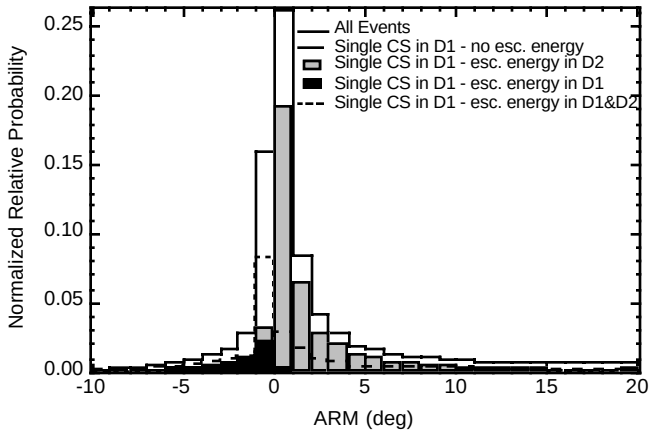

Figure II.14 The simulated ARM distribution for a 12.140 MeV monoenergetic point source at normal incidence.

II.E. CDG Effective-Area Calculation

COMPTEL only measures the individual photon energy deposits and interaction locations. To measure a flux of gamma rays one needs additional information such as the duration of the measurement, the energy bin size and the effective area or the absolute response of the

instrument. During calibration it was not possible to measure the COMPTEL response to a diffuse source in the laboratory. Therefore, we calculate the instrument response using Monte Carlo simulations of a diffuse source. Complications due to photons scattering in and out of the incident beam, secondary photon production in the surrounding inactive material and from the shadowing of active detectors at large zenith angles are taken into account in the simulation. In this work the simulated cosmic diffuse source refers to a 2π isotropic source having a power-law distribution in energy.

For calculating the effective area using simulations, we rewrite the effective area A_{eff} as

$$A_{eff}(\theta,\varphi,E) = \frac{C_{src-detected}}{I_{src-beam}} = \frac{\text{detected photons}}{\text{source photons/cm}^2} \tag{2.4}$$

where $C_{src\text{-}detected}$ is the number of source photons detected after applying identical data selections to the simulations as we do with the data. The $I_{src\text{-}beam}$ is the simulated photon-flux from the source per unit area incident on the detector. The source flux $I_{src\text{-}beam}$ represents a parallel wave front of photons from the source and is defined as

$$I_{src-beam} = \frac{C_{src-input}}{A_{src-beam}} \tag{2.5}$$

where $C_{src\text{-}input}$ is the number of source photons incident and A_{beam} is the simulation beam area. To get the correct response it is necessary to have $A_{beam} >> A_{geo}$ (to account for effects such as scattering of the incident photons in and out of the beam), with the source flux being uniform within A_{beam}.

For point sources the effective area, reduces to

$$A_{eff} = \frac{C_{src-detected}}{I_{src-beam}} = \frac{C_{src-detected}}{C_{src-input}} \times A_{beam} \tag{2.6}$$

Note that when $A_{beam} = A_{geo}$, then A_{eff} reduces to the familiar form, $A_{eff} = \varepsilon \times A_{geo}$, the product of intrinsic efficiency with the projected geometric area (the definition in equation 2.3).

For a diffuse source the total response (in units of cm^2-sr) is determined by integrating A_{eff} over the solid-angle subtended by the source. Hence, for a diffuse source

$$A_{eff} = \int_{\Omega_{src}} A_{eff}(\Omega)d\Omega = \int_{\Omega_{src}} \frac{C_{src-detected}}{I_{src-beam}}(\Omega)d\Omega \tag{2.7}$$

If the simulation beam area A_{beam} is the same for all directions (any θ and ϕ across the source) and the source flux I_{src} (photons per unit area) is constant within this beam area, then the integration for A_{eff} once again simplifies to the product of intrinsic efficiency averaged over the source beam area and the solid-angle subtended by the source:

$$A_{eff} = \int_{\Omega_{src}} d\Omega \times \frac{C_{src-det}}{C_{src-input}}(\Omega) \times A_{beam} = A_{beam} \times \Delta\Omega_{src} \times \left\langle \frac{C_{src-detected}}{C_{src-input}} \right\rangle \tag{2.8}$$

Usually, A_{eff} is computed for some energy bin, $C_{src\text{-}detected}$ and $C_{src\text{-}input}$ are the number of detected and incident photons in the energy bin, and $\Delta\Omega$ is the solid-angle subtended by the source. Note that the uniform source flux and fixed beam area at all angles that simplifies the integration.

The real CDG radiation is assumed to be constant and isotropic. The CDG response is determined for a 2π isotropic source simulation since the data from only downward-moving gamma-ray events are analyzed. The algorithm is outlined below.

(1) Pick a random direction (θ_1,ϕ_1) from a hemispherical (2π) distribution centered at D1. The hemispherical distribution has the proper solid-angle weighting required for a 2π isotropic source. The angle ϕ_1 is chosen randomly from a uniform distribution between 0 and 2π while the angle θ is chosen randomly from a $\cos(\theta_1)$ distribution between 0 and 1.

(2) A rectangular beam of cross-sectional area A_{beam}, independent of the photon direction, is chosen perpendicular to the (θ_1,ϕ_1) direction. The rectangle is placed outside the veto1 dome and has an area larger than the projected D1 geometrical area (A_{beam} = 28,236 cm^2).

(3) A random position (x,y,z) outside the veto-domes is then chosen within the rectangular beam. This defines the trajectory of the incident photon.

(4) A random photon energy ε_0 is drawn from a power-law distribution of photon energies.

(5) The simulation begins at the position (x,y,z) with the incident photon traveling towards D1 in the direction (θ_1,ϕ_1) with energy ε_0.

The number of trial photons N_{input} and the triggered event parameters are recorded. The simulated events are subject to the same data selections as those in the measurements. For a given data selection, with $C_{detected}$ simulated events passing all selections in an energy interval ΔE, the effective-area A_{eff} (in units of cm^2-sr) is:

$$A_{eff} = \frac{C_{detected}}{N_{input}} \times A_{beam} \times 2\pi \tag{2.9}$$

The CDG effective area is computed using an $E^{-2.5}$ power-law from a 2π isotropic source simulation. The resulting effective area is shown in figure II.15 as a function of energy, for the case of *standard CDG* data selections (defined in section IV.C). The general shape of A_{eff} with energy for diffuse sources is similar to the case for point sources (see figure II.4).

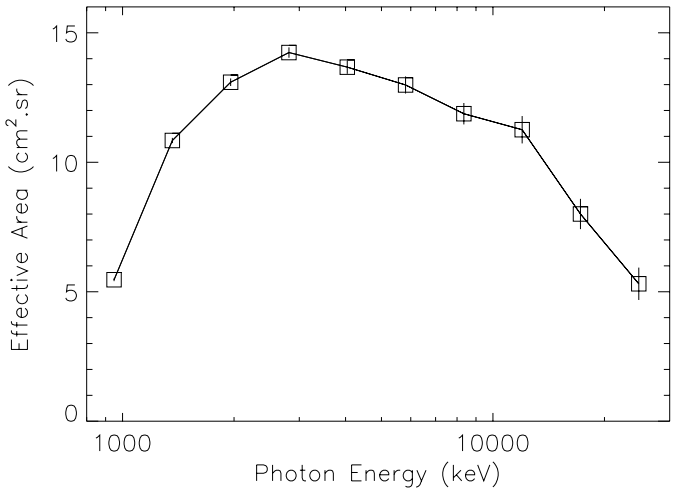

Figure II.15 The CDG effective area computed using an $E^{-2.5}$ power-law and a 2π isotropic source for standard-CDG event selections.

The incident CDG source-flux $(cm^2\text{-s-sr-MeV})^{-1}$ is computed as follows

$$\text{Flux} = \left(\frac{C}{\Delta t}\right) \times \frac{1}{\Delta E} \times \frac{1}{A_{eff}} \tag{2.10}$$

where C is the CDG-counts, Δt is the measurement duration (s), ΔE is the energy bin (MeV) and A_{eff} is the effective area (cm^2-s).

II.F. Time-of-Flight Corrections

As we shall see in the chapter on the Instrument Background, the time-of-flight (ToF) measurement is one of the most powerful tools to distinguish the signal from the background. However, the raw ToF measurement is not the best ToF value for scientific analysis. The raw ToF suffers from many effects that tend to broaden the ToF resolution. For example, there is a ToF uncertainty due to the fact that each of the minitelescope (D1-D2 module combination) has a different path-length (a geometric effect that shifts the ToF peak up to 10 channels). We also observe a *ToF walk* with the analog sum of the PMTs from D1 and D2 (related to the energy deposit in the individual detectors). A better ToF resolution will result in a narrower ToF range for good events, increasing the signal-to-background (S/B) ratio of our measurements.

The basic approach is to examine the behavior of the ToF forward-peak for Earth observations, since the Earth is bright in gamma rays and produces a large signal in the forward peak. Algorithms were developed to align the forward peak at channel 120 and correct for the observed ToF trends to improve the resolution (van Dijk 1996). The resulting ToF corrections are then applied to all the data before analysis. The TCFCOR ToF corrections (van Dijk 1996), are applied to all the EVP data used in this work. The TCFCOR ToF corrections accounts for the following ToF problems:

The minitelescope dependence: These variations in the ToF forward peak position are due to the differences in the interaction path-lengths between the D1 and D2 detector planes and the module cable-lengths that carry the ToF signals. The corrections normalize all events to a fixed path length and shift the trigger times so that all down-scattered events fall at channel 120.

The D1 and D2 analog sum dependence: The analog sum refers to the total PMT amplitude from a module (in volts) and represents a measure of the total energy deposit within the module. The ToF-trigger times show a strong modulation with the summed PMT signal (analog sum). We observe that lower energy deposits result in a slower (delayed) ToF trigger whereas larger energy deposits result in faster (earlier) ToF triggers. For example, events with lower E1 and higher E2 result in shorter ToF values while events with higher E1 and lower E2 result in longer ToF values. The ToF peak position was determined for fine D1 and D2 analog sum bins and the measured ToF

walk was characterized by polynomials. The fits are used to align the forward-peak position for any E1/E2 analog sum (energy) combination.

The detector temperature dependence: There is a linear relationship between the temperature of the detector and the position of the forward peak. The ToF dependence on detector temperature is corrected by normalizing all events to a fixed temperature (20˚ C).

The module threshold dependence: The D1 and D2 detectors have different thresholds ranging from 0–7, with 7 corresponding to the lowest energy threshold. The TCFCOR corrections determine analog sum corrections depending on the D2 hardware threshold level.

The sub-D1 module dependence: Compared to an interaction in the center of the D1 detector module, a large energy deposit near one of the PMT windows results in an early ToF trigger that shifts the ToF peak position to higher channels. A map of the ToF peak positions has been produced for a single D1 module (D1-7). This map has been used to correct for the D1 interaction position within all the D1 modules.

Henceforth all references to a ToF measurement will refer to the corrected ToF measurement. Although these TCFCOR corrections account for most the ToF walk and significantly improve the ToF resolution, the forward-peak position may still be shifted up to ~2 channels away from channel 120 in certain energy ranges. This appears to be due to the different geometry of the instrumental background that has a ToF signature different than the scattered-photon events. The shifts in ToF-peak position is a result of the energy dependent contribution of the instrumental background to the overall count rate. In section III.D I will discuss the composition of the ToF spectrum in terms of event-mechanism and event-geometry. I will present the behavior of the ToF spectrum as a function of total energy in section V.A.

II.G. The Veto System

At the nominal altitude of 450 km, COMPTEL is continuously bombarded by a large flux of high-energy cosmic-rays and other secondaries produced in the spacecraft and the Earth's atmosphere. The charged-particles can directly interact with the scintillating material in the D1 and D2 detectors via the ionization process and suffer energy losses. In general, it is not possible to distinguish between the energy loss due to charged particles from the energy loss due to

photons. The COMPTEL veto subsystem is designed to identify detector triggers due to energy deposits from charged-particles and suppress these events.

Each of the D1 and D2 detector assemblies is completely surrounded by two separate active plastic charged-particle shields called veto domes. These are used in anti-coincidence with D1 and D2 detectors to reject charged-particle interactions. The anti-coincidence requirement means that when the veto domes detect a charged-particle event, then the telescope-event logic circuit between the D1 and D2 modules are blocked for a short time (~130–170 ns) to allow for the passage of the charged particle through the instrument, ignoring any possible D1 or D2 triggers during this time.

Each of the four veto domes are Cassini-shaped and made of a thin (1.5 cm thick) plastic scintillator (NE 110). Each of the four veto domes is viewed by 24 PMTs that are optically coupled to the cylindrical edge of the dome. In order to completely shield the detectors there is an overlap between the two veto-domes that surround each detector assembly. For each veto dome the sum of the 24 PMTs is processed by its own low-level discriminator. The fast-logic output of these discriminators is used by the fast-coincidence circuit for anti-coincidence processing.

During calibration the efficiency for each veto dome to reject charged particles was tested by using atmospheric muons as test particles. The measured rejection efficiency was greater than 99.9% for all veto-domes. The 1.5 cm thick plastic veto domes correspond to 0.71 g/cm^2 of material. The absorption-length for the plastic is about 85 g/cm^2, therefore most photons pass through without suffering energy loss. The radiation-length for the plastic is about 41 g/cm^2, therefore charged particles passing through will not radiate inside the domes. The small thickness of the veto domes does not significantly attenuate the gamma rays, yet they are nearly 100% efficient in detecting charged particles by ionizational energy losses.

Veto-scalers versus Veto-rates

In the veto subsystem the signal is gated with a clock pulse of 50 ns (τ_{clock}) at a clock frequency of 312.5 kHz (f_{clock}). The resulting coincident pulses for each veto dome are accumulated separately for 2.048 seconds in each superpacket (16.384 s) and the resultant scalers are recorded in the HKD datasets as *veto-deadtime scalers*. The individual veto rates are then be determined from the veto-deadtime scalers according to the deadtime-meter principle.

The veto triggers are distributed randomly in time and randomly coincide with the clock pulses. Therefore, the fractional deadtime computed during the clock pulses is also applicable to the times between the clock pulses. Thus, the fractional deadtime during the clock on-time is the fractional deadtime for the entire superpacket.

A clock pulse of 50 ns at 312.5 kHz means one clock pulse every 3200 ns. The total fractional clock pulse-time is equal to the product of the clock-pulse time (τ_{clock}) and the clock-pulse frequency (f_{clock}). Therefore,

$$\text{fractional clock-pulse time} = 50\ \text{ns} \times 312.5\ \text{kHz} = 0.016 \tag{2.11}$$

Although the total clock-pulse time is small (1.6%), its fractional deadtime is accurate. The fractional deadtime can be computed as,

$$\text{veto-deadtime (\%)} = 100 \times (\text{veto-deadtime}/2.048\text{s}) / 312.5\ \text{kHz} \tag{2.12}$$

The deadtime-meter principle states that,

$$\text{coincidence-rate (1/s)} = \text{rate1 (1/s)} \times \text{rate2 (1/s)} \times \tau_{coincidence}\ \text{(s)} \tag{2.13}$$

where $\tau_{coincidence}$ is the coincidence-pulse time. In the veto2 subsystem this translates into,

$$\text{veto2-deadtime}/2.048\ \text{s} = \text{veto2-rate (1/s)} \times 312.5\ \text{(kHz)} \times \tau_{coincidence}\ \text{(s)} \tag{2.14}$$

The deadtime-meter principle is true for all veto-deadtime rates, but the conversion from veto-deadtime scalers into veto rate is accurate only when the veto-deadtime fraction is much smaller than 100%. This is because the veto-deadtime scalers also reflect the amount of deadtime of the veto detectors themselves. The highest value for the veto2-deadtime scaler is ~2500, implying a maximum deadtime fraction of less than ~1%. Thus, the deadtime-meter principle is valid for all values of the measured veto2-deadtime scalers. The coincidence-pulse-time $\tau_{coincidence}$ is the sum of the clock-pulse time, τ_{clock} (50 ns) and the veto pulse, $\tau_{veto\text{-}signal\text{-}pulse}$ (130–170 ns). Therefore,

$$\tau_{coincidence} = \tau_{clock} + \tau_{veto\text{-}signal\text{-}pulse} \sim 50\ \text{ns} + 200\ \text{ns} = 250\ \text{ns} \tag{2.15}$$

The coincidence-pulse width is around 250 ns, therefore there are about 12.8 (=3200/250) veto pulses between two consecutive clock pulses. So, on average we are counting the veto2-deadtime scalers only once out of every 12.8 veto-triggers, as predicted by the deadtime meter principle. We now have the relationship between the veto2-deadtime scalers and the veto2 rates,

$$\text{veto2 rate [1/s]} = 12.8 \times (\text{veto2-deadtime}/2.048\text{s}) \tag{2.16}$$

Basically, while veto2-deadtime << 312500 (as is in our case), the veto2 rate is proportional to the veto2-deadtime scaler. This means that the veto2-deadtime scaler is equivalent to the veto2 rate. I will use the term veto scaler and veto rate interchangeably throughout this work.